Contents lists available at ScienceDirect

Applied Materials Today

Zeolite templated carbon from Beta replica as metal-free electrocatalyst for CO$_2$ reduction

G. Papanikolaou [a,*], D. Chillè [a], S. Abate [a], S. Perathoner [a], G. Centi [a], G. Giorgianni [b], D. Cozza [b], F. Dalena [b], M. Migliori [b], G. Giordano [b], P. Lanzafame [a]

[a] *Department of Chemical Biological Pharmaceutical and Environmental Sciences (ChiBioFarAm) – Section of Industrial Chemistry, University of Messina, ERIC aisbl and INSTM CASPE, V.le F. Stagno d'Alcontres 31, 98166 Messina, Italy*
[b] *Chemical Engineering, Catalysis and Sustainable Processes Laboratory – CECaSP_Lab, University of Calabria, Rende (CS) 87036, Italy*

ARTICLE INFO

ABSTRACT

Zeolite Templated Carbons (ZTCs) are a class of materials that feature the textural properties of the template zeolites and the high conductivity of graphene-like structures. These characteristics make ZTCs a valuable candidate for CO$_2$ catalytic reduction. We report here for the first time that metal-free ZTCs obtained from Beta zeolite are a novel valuable energy material for the reduction of CO$_2$ to formic acid, about 10 times better than a reference reduced graphene oxide catalyst. In addition, it is evidenced that the pristine ZTC contains a large amount of oxygen, an aspect largely underestimated in literature. A specific method to reduce this oxygen content was developed, that coupled to an in-depth characterization by multiple techniques of these materials, allows to understand the nature of the oxygen functionalities on ZTCs surface. Moreover, it was evidenced that the change of oxygenated species by combined thermal and NaBH$_4$ treatment of ZTCs affects the catalytic behavior, leading to a remarkable increase in the performances compared to the pristine one. The comparison of the performances and characteristics of two ZTCs, obtained by different BEA nanostructures, allow to correlate better the modification of the type of oxygen species present in ZTCs to the catalytic behavior. The results open new perspectives for the catalytic application of deoxygenated ZTCs.

1. Introduction

The development of novel energy materials for the electrocatalytic conversion of small molecules as CO$_2$ is one of the research areas with the faster growing of interest both academic and industrial because is an effective green strategy to reduce the carbon footprint of the chemical production [1–4]. However, the electrocatalytic reduction of CO$_2$ (CO$_2$RR), similarly to other electrocatalytic applications of large recent research interest (such as the N$_2$ conversion to NH$_3$), still represents a challenge to meet the performances for industrial exploitation [1,5–8].

Among the different products of CO$_2$RR, formic acid (FA) is one of the chemical substance of largest research interest [9,10]. While most of the studies on this electrocatalytic reaction use electrodes containing metal nanoparticles as the electrocatalytic element, for example (Pd, Pt, Ag, and Au) [11–13], transition (Fe, Ni, Cu, and Zn) [14–19], and p-block metals (In, Sn, Pb, and Bi) [20–23], to avoid their presence is a valuable target to reduce costs, the pos-

sible leaching (improving stability) and enhance the process sustainability. For this reason, there is an increasing interest in developing metal-free electrocatalysts [3,5]. Carbon materials, for their (often) good electrical conductivity and the possibility to prepare in a large-range nanostructures with tailored properties, have been also studied extensively as metal-free catalysts including in electrocatalytic CO$_2$RR [24–32], although the nature of the active sites is still controversial. A characteristic scarcely explored for these metal-free nanocarbons, at least as electrocatalysts, is the possibility to develop electrocatalysts having a structure replica of zeolites, and thus an ordered nanostructure with cavities of molecular dimension. As for zeolites, the confinement within the pores of this nanomaterial can induce a better control of the reactivity, and the development of high surface area nanostructured electrodes. Focusing the studies on this topic represent a new direction to develop novel materials for electrocatalysis [3].

Zeolite-Templated Carbons (ZTCs) exhibit an ordered microporous structure, extensive surface areas (up to 4000 m^2/g) with a large density of edge sites (about 10-times larger than conventional activated carbons), a high electrical conductivity due to its sp^2-hybridized carbon network with a graphene-like structure, are

---

* Corresponding author.
E-mail address: gpapanikolaou@unime.it (G. Papanikolaou).

promising candidates for the development of electrocatalysts with improved properties [33–35]. Although their structure is formally the replica of the parent zeolite, the obtained structure is more complex and started to be understood only recently [36,37]. In general, ZTCs are characterized by an ordered three-dimensional network of pores contained between atomically thin, polycyclic hydrocarbon walls (formed during the carbonization process within a zeolite template). However, a range of highly defective carbon nanostructures (characterized by two-sided, ribbon-like open-blade" connectors [36]) is possible, in agreement also with the high surface area.

A large amount of oxygen can be present in the ZTC materials in order to compensate the presence of defects, but the amount and nature of these oxygen functionalities depends strongly on the preparation methods [38]. The presence of oxygen functionalities in ZTC materials may significantly affect their electrocatalytic behavior, influencing the surface polarity, the conductivity and the nature of the reactive sites. In other type of carbon materials, the presence of oxygen functionalities, often induced by specific oxidative treatments, is widely reported and ascribed to the significant portion of sp^3 carbons [26,39,40]. Nishihara et al. [41] examined the amount and the type of oxygen functional groups on ZTCs synthesized in the nanochannels of zeolite Y by FT-IR spectroscopy and temperature-programmed desorption tests at different temperatures, although the influence of these species on the electrocatalytic properties was not investigated. In ZTCs, oxygen functionalities are probably formed after the zeolite template dissolution procedure by acidic or basic hydrolysis and can be related to the considerable strain in the 3D curved graphene-like structure formed inside zeolite nanopores [42]. In general, these oxygen functionalities may have different possible effects on the electrocatalytic properties, acting for example as active centers [30] but also reducing the electrical conductivity of the material and thus the electrocatalytic behavior. In general, it has been shown that the increase of the reduction degree by restoring sp^2 hybridization improves the conductivity of these materials, enhancing their features as electrocatalysts [43]. Also the wettability of the electrocatalysts could be influenced from the amount and nature of the oxygen functionalities. Therefore, controlled and combined thermal and reducing treatments could change the nature of the oxygen functionalities present on ZTCs and in turn the electrocatalytic behavior. However, this aspect was not investigated.

Metal-free ZTC materials are thus a potential interesting type of novel electrocatalysts, but many aspects have to be investigated to understand these complex nanomaterials. We focused attention on Beta structure replica ZTC, because comparatively less studied with respect to other zeolite replica such as Y. Zeolite Beta is an example of stacking disorder being a highly intergrown hybrid of two distinct, but closely related structures (polymorph A and B). Their ratio depend on the specific preparation characteristics of the zeolite. The carbon replica could be likely affected from a change in this polymorph ratio being the ZTC formation impacted from the crystal size and the lattice strain of the zeolite template [44,45].

Therefore, we have studied here two ZTC samples prepared as replica of two differently prepared zeolite Beta, although with closely related characteristics (as Si/Al ratio and nanocrystal dimensions). These ZTC materials were investigated before and after a combined thermal/reductive treatment to change the nature/amount of oxygenated functionalities. The investigation combines the characterization of these materials by various methodologies to the analysis of their electrocatalytic behavior in the electrocatalytic reduction of CO_2 to formate. These tests were made under industrially relevant conditions, using an electrocatalytic flow cell. A reduced graphene oxide (rGO), presenting a prevalently sp^2-hybridized carbon framework, was used as a comparison and reference providing a direct way to compare the role of 2D and 3D
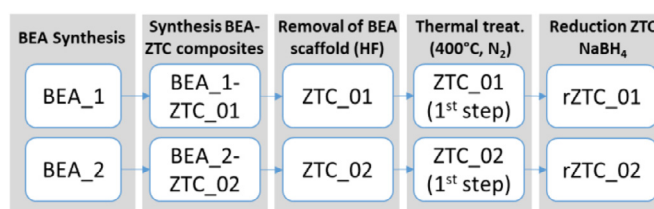

Fig. 1. Scheme of the preparation of ZTC Beta replicas.

carbon nanostructures. Several studies have been reported in the literature on rGO-based electrodes [46], including for CO_2 reduction [47].

The results provide some new insights on the use of ZTCs from Beta replica as metal-free electrocatalyst for CO_2 reduction.

2. Experimental

2.1. Materials

2.1.1. ZTC synthesis

Two different BEA samples were used as scaffold for ZTC synthesis: one of them was syntesised in hydrothermal condition (see Supplementary Information), according to the procedure previous reported in literature [48] and the carbon replica obtained from this sample was labeled as ZTC_01. The second one was a commercial BEA with a similar Si/Al ratio (Si/Al$_{bulk}$=39) (Zeolyst International, USA) and the series of ZTC produced using this scaffold was labeled as ZTC_02.

Using zeolites in Na$^+$form as template scaffold, all ZTCs were synthetized via Chemical Vapor Depositions (CVD) at 700 °C using ethylene as a carbon source according to a previously published procedure [49]. The obtained carbon phase was extracted from the carbon-zeolite composite by dissolving the zeolite framework in HF (48%, Merk) and, then, in HCl (38%, Carlo Erba) stirring the suspension at r.t. for 15 and 6 h, respectively. Afterward, the carbonaceous phase was filtrated, washed with abundant distilled water, and dried at 90 °C overnight.

2.1.2. Surface modifications of ZTC

The prepared ZTCs were deoxygenated using a two-step procedure. In the first step, the prepared ZTCs were treated under nitrogen at 400 °C for 3.5 h [41]. Then, in the second step, the thermally treated ZTCs were dispersed in water (5 mg/mL) and chemically reduced with NaBH$_4$ (10 mg/mL - Acros Organics, 98%), using a method adapted from the preparation of rGO [50]. After the NaBH$_4$ addition, the suspension was stirred at r.t. for 20 min. Then, it was heated at 70 °C and kept in constant stirring at this temperature for 3 h. At the end of treatment, the suspension was filtered, washed sequentially with abundant distillate water and acetone and dried at 90 °C overnight. The samples obtained from this combined thermal and NaBH$_4$ treatment procedure are named rZTC_01 and rZTC_02, respectively, in the following of the paper. Fig. 1 summarizes schematically the various steps of the procedure and the name of the samples.

2.2. Textural and spectroscopic characterization

The efficiency in removing the templating zeolitic structure of the post-synthesis acidic treatment was evaluated by thermogravimetric analysis (TGA) (TA Instruments SDT 650) of the purified ZTC, heating the sample up to 1000 °C (heating rate of 5 °C·min^{-1}) under air flow. The same equipment was also used for the TGA studies of ZTC materials in inert atmosphere with a linear temperature increase (5 °C/min).

XRD data were collected by a powder XRD (Rigaku Miniflex 600, Cu tube) in the 2θ range of 5–50° with angular step size of 0.02° and acquisition rate of 1°·min^{-1}.

The Oxygen/Carbon molar ratio was measured by a Scanning Electron Microscopy (SEM, LEO 420) coupled to an Energy-Dispersive X-ray spectroscopy (EDX, Inca Energy System, Oxford Instruments) under the following experimental conditions: $6 \cdot 10^{-6}$ torr, 650 pA, 15 kV, working distance of 19 mm. The samples were metallized with gold in order to preserve it from the high energy electron beam and the gold peak was removed by post processing data analysis. Each sample was measured six times in different areas (50 μm in size).

Textural properties of the pristine and surface-modified ZTCs were estimated by N_2 physisorption at 77 K (ASAP 2020 Micromeritics). Before analysis, the samples were degassed at 50 μmHg and 30 °C. Then, the temperature was raised to 350 °C and maintained for 6 h. Specific surface areas, microporous volume and area were estimated by the Rouquerol transformed BET (Brunauer, Emmett and Teller) and t-plot methods [51]. The pore size distribution of the prepared ZTCs was evaluated by using the HS-2D-NLDFT method, developed for N_2 adsorption on carbon-based materials presenting slit-like pores of infinite size [52].

FT-IR spectra of the pristine and surface-modified ZTCs were measured using a Nicolet iS 10 (Thermo Scientific, U.S.A.), equipped with a DTGS detector. ZTCs samples were grounded for 15 min, diluted in KBr (0.2 wt.%), and pressed as self-supporting wafers (13 mm diameter), using a hydraulic press (10 ton). Then, the prepared ZTC wafer was dehydrated at 105 °C for 1 h, stored in a desiccator, and investigated at r.t. in the mid-infrared region (4000–400 cm^{-1}), with an optical resolution of 4 cm^{-1}.

Raman spectroscopy of carbon-based electrocatalysts was performed using a DXR^{TM} 3xi Raman Imaging Microscope (Thermo Scientific) with 900 lines/mm and a laser wavelength of 532 nm for an exposure time of 180 s per spectrum.

XPS spectra were recorded using a PHI VersaProbe II (Physical Electronics), equipped with an Al Kα (1486.6 eV) X-ray source. The survey spectra were recorded with an analyzer energy path of 117 eV, while the C1s and O1s core levels were measured at 23.5 eV. The X-ray beam size was 100 μm at 25 W. The position of the XPS peaks was referenced to Au foil (84 eV). XPS peaks were deconvoluted using the Multipack Data Reduction Software (ULVAC-PHI, Inc), employing a Shirley background curve.

2.3. Carbon-based/gas diffusion electrode fabrication

The working electrodes based on Gas Diffusion Electrode (GDE) configuration were prepared by deposing the metal-free carbon-based electrocatalysts (ZTC_01, ZTC_02, rZTC_01_ rZTC_02, rGO) on Gas Diffusion Layer (GDL, 29 BC Sigracet®) with a geometric area of 10 cm^2. An ink was prepared by dispersing the pristine, the surface-modified ZTCs and the rGO in a Nafion/ethanol solution (40 μL, 10 wt.%) where Nafion was used as a binder. The resulting ink was sonicated for 20 min and then deposited onto GDL to obtain a final loading of 0.5 mg/cm^2. The ZTC ink was sprayed on the GDL laying on a heating plate set at 150 °C, using an airbrush to speed up solvent evaporation and to obtain a homogenous catalytic layer.

2.4. Electrochemical measurements

CO_2RR behavior was studied at room temperature and pressure using a Micro Flow electrochemical Cell (purchased from ElectroCell) powered by potentiostat galvanostat (Autolab Pgstat302n Metrohm). The electrocatalytic cell was in a three-electrode cell configuration, using the prepared carbon-based electrodes as a working electrode (WE), an Ir/Ru DSA plate as counter electrode, and a 1 mm leak-free Ag/AgCl (3.4 M KCl) electrode as a reference. The cathodic compartment was physically separated from the anodic one by a proton exchange membrane Nafion® 115 (by Fuel Cell Store), previously treated with H_2O_2 to remove organic impurities and then activated with a 0.5 M H_2SO_4. The external catholyte and anolyte tanks (filled with 40 mL of 0.5 M of $KHCO_3$ and 0.5 M of H_2SO_4, respectively) were connected to the flow cell. The electrolyte was flowed to the cathodic and anodic chamber with a 15 mL/min flow rate, using a peristaltic pump. Prior the electrocatalytic tests using CO_2, blind trial tests were carried out by saturating the $KHCO_3$ electrolyte with Ar at different potentials in order to exclude the possible contribution to the liquid products formation deriving from the electrolyte. Pure CO_2 was flushed through the GDE working electrode with a flux rate of 10 mL/min and released into the catholyte tank. A scheme of the cell configuration is reported in Fig. 2.

Cyclic Voltammetry (CV) was performed within the potential range from 0.5 to -2.0 V (vs. Ag/AgCl) at a scan rate of 50 mV·s^{-1} in both Ar or CO_2 environment.

The electrocatalytic behavior of the carbon-based/GDE in CO_2RR was evaluated through chronoamperometric measurements, carried out for 60 min at two potentials, namely -1.6 V and -1.8 V vs. Ag/AgCl. In order to obtain the reproducible results, all the measurements were performed at least in duplicate.

A 3D High-Performance Liquid Chromatography System (HPLC Shimadzu Nexera-I LC-2040C), equipped with an Aminex HPX-87H Column and a photo diode array (PDA) detector, measured the reaction products in the liquid phase, while an on-line Agilent 490 micro gas-chromatograph (Micro GC) equipped with a Molsieve 5 Å and a PoraPLOT Q columns, measured the gas phase products.

3. Results

3.1. Structural and textural characterization

The structural and textural properties of the starting Beta zeolites (BEA_1, BEA_2) were analyzed. Data are reported in the Supplementary Information (Figs. S.1 and S.2, Table S.1). Both zeolites present a similar values of the Si/Al ratio in the zeolite bulk (about 39) and of crystallite size (18–20 nm). However, while XRD peak at about 22.5° is well coincident for the two samples, the reflection at about 7.8° results assymmetric (a shoulder is present at about 7.2°) and slightly less intense in BEA_1 compared to BEA_2. This is consistent with a change in the amount of Beta polymorphs ratios between BEA_1 and BEA_2 samples [53]. The porosimetric analysis evidences a more pronounced mesoporosity of the commercial BEA_2.

The thermo-gravimetric analysis (TGA) of the pristine ZTCs (Fig. 3) indicates complete carbon combustion after 650 °C. Therefore, the total zeolite matrix dissolution after HF/HCl treatments can be inferred. The derivative thermogravimetric curve profile also reveal a single convoluted peak around 540 °C, indicating the presence of at least two different carbon species.

The XRD patterns of prepared Na-BEA, pristine, and treated ZTCs after background subtraction are reported in Fig. 4. The Na-BEA XRD pattern shows the typical diffraction reflections of the BEA framework, high phase crystallinity, and purity. The two major peaks at 8 and 15° in the pristine ZTCs indicate a neat replica of the zeolite framework. Although ZTCs are not crystalline materials, and their diffraction patterns are only the results of the periodic ordering of atoms within periodic surfaces [54], their apparent crystallinity can be evaluated using the most intense reflections, as reported for zeolites. Taking the intensity of 8° reflection as a reference, the crystallinity of prepared ZTCs, decreased in the order ZTC_02 > ZTC_01 > rZTC_02 > rZTC_01 from 100% to 50% (see inset in Fig. 4). Moreover, a similar trend was shown by the

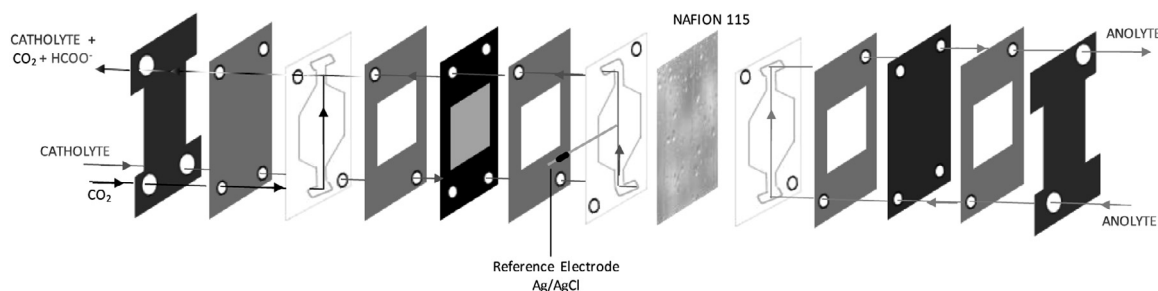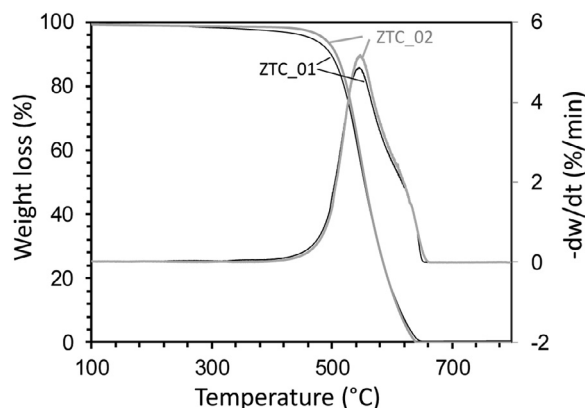**Fig. 2.** Scheme of the electrocatalytic flow cell.

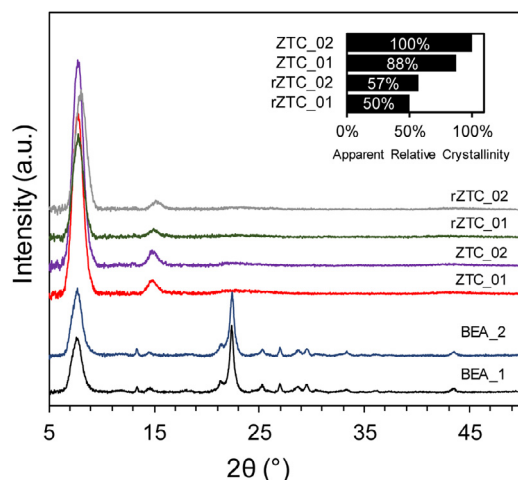**Fig. 3.** TGA and derivative thermogravimetric curve profiles of pristine ZTC samples.

Fig. 4. XRD pattern of Zeolite template (NaBEA), pristine (ZTC_01 and ZTC_02) and NaBH$_4$ treated (rZTC_01 and rZTC_02) ZTC samples. Apparent crystallinity of the samples (Inset).

15° reflection. By testing the effect of the bare NaBH$_4$ reduction treatment no amorphization was observed. Instead, after the bare annealing treatment at 400 °C the apparent relative crystallinity decreased [33,54]. Therefore, the amorphization of the treated ZTC can be related to the sole annealing.

EDS data confirmed that the performed combined thermal and reduction treatments reduce the amount of oxygen in the ZTC samples (Table 1) with a O/C ratio reduction of 38% and 33%, with respect to the pristine forms, for rZTC_01 and rZTC_02 respectively.

Thermogravimetric (TGA) data (Fig. 5) of ZTC_01 evidence clearly the presence of multiple type of oxygen species in the samples, which, after annealing at 400 °C in inert flow (N$_2$) are reduced to two main species which decomposition is centered at

about 560° and 660 °C, the latter broader. They can be attributed to lacton and ether or phenol species, respectively. After the treatment with NaBH$_4$, however, there is a relative intensification of the decomposition peak centered at about 560 °C, and the reformation of some of the lower temperature decomposition peaks present in the not-annealed ZTC_01, especially a well defined decomposition peak centered at about 420 °C indicative of lactons or anydride species. In the rZTC_02 (Fig. 5b), in comparison with rZTC_01 these two decomposition peaks centered at 420 °C and 560 °C are instead of minor intensity with the main decomposition peak being centered at about 560 °C with a shoulder at higher temperature (about 760 °C). Therefore, rZTC_01 and rZTC_02 show clearly the presence of different oxygen functionalities.

N$_2$ physisorption isotherms at 77 K of the ZTC samples (Fig. 6a) presents Type I isotherms with minor contributions of the type IV isotherms, with a small hysteresis loop closing between 0.8 and 0.9 p/p°, typical of microporous materials in the presence of small fraction of meso and macropores. The textural properties, as calculated by conventional and NLDFT methods, taking into account the presence of negligible systematic deviations, agree with each other (Table 1). After synthesis, the ZTC_02 sample (Table 1) exhibits the largest specific BET (S_T^{BET}), microporous (S_μ), external (S_m) surface areas, and also the largest total (V_p), microporous (V_μ) and mesoporous (V_{meso}) volumes. Conversely, with respect to the ZTC_02 sample, the ZTC_01 shows a similar external surface area and lower BET surface area (-5%), microporous surface areas (-5%), total pore volume (-8%), and microporous volume (-6%). After the combined thermal annealing and NaBH$_4$ treatment both samples show a decrease of all the above-mentioned textural properties, with the ZTC_02 sample presenting the most extensive decrease. More specifically, the rZTC_02, compared with the ZTC_02, showed a 15, 16% decrease in both the BET and microporous surface areas, while the mesoporous area, apparently, increased by 4%. The total and microporous pore volumes, instead, decreased by 16, 17% each. Conversely, after the two-step deoxygenation procedure, the mesoporous surface areas and volumes of the ZTC_01 sample decreased by 56 and 30%. The textural properties did not change significantly after the bare chemical treatment, but only after the 400 °C annealing treatment (data not shown). The latter agrees with the data reported by Choi et al. [55,56], reporting, for BEA-ZTCs, a substantial decrease of specific surface areas and pore volumes after annealing at 600 and 800 °C. From the NLDFT pore size distribution analysis, two main families of micropores can be identified in all the analyzed samples (Fig. 6b). The most abundant micropore family was centered at 0.9 nm and is in the same range as the calculated structures of ZTCs [55,56]. The second pore family was observed at 0.12 and 0.20 nm.

In the case of the ZTC_01 sample, after the two-step deoxygenation treatment, the median diameter of the first micropore family decreased from 0.908 ± 0.005 to 0.894 ± 0.004 (95% confidence interval) and for the ZTC_02, from 0.908 ± 0.005 to 0.900 ± 0.005, in agreement with Choi et al. [55,56]. Conversely, the full width

Table 1
O/C ratio and textural properties of the pristine and NaBH$_4$ treated ZTC samples.

Sample	O/C (mol/mol)[a]	S_T^{BET}[b] (m^2/g)	S_μ[b]	S_m[b]	V_p[b] (cm^3/g)	V_μ[b]	V_m[b]	S_T^{DFT}[c] (m^2/g)	S_μ^{DFT}[c]	S_m^{DFT}[c]	V_p^{DFT}[c] (cm^3/g)	V_μ^{DFT}[c]	V_m^{DFT}[c]
ZTC_01	0.194 ± 0.018	2020 ± 26	1927	93	1.22	1.02	0.20	2005	1938	67	1.18	0.944	0.236
rZTC_01	0.119 ± 0.021	1913 ± 28	1872	41	1.10	0.96	0.14	1896	1874	22	1.05	0.913	0.136
ZTC_02	0.163 ± 0.013	2126 ± 28	2033	93	1.33	1.09	0.24	2113	2041	72	1.34	1.011	0.326
rZTC_02	0.109 ± 0.024	1798 ± 27	1701	97	1.11	0.92	0.19	1826	1747	79	1.10	0.845	0.255

[a] Calculated by EDS measurements

[b] S_T^{BET}: Specific total surface area calculated using the BET and Rouquerol transform V_μ, S_μ, and S_m: specific microporous volume, area, and external or mesoporous surface areas calculated using the t-plot, and the Harkins and Jura curve, in the t-range 0.7-1.1 nm; V_p: total pore volume measured at p/p° 0.97 from the adsorption isotherm.

[c] S_T^{DFT}, S_μ^{DFT}, S_m^{DFT}, V_p^{DFT}, V_μ^{DFT}, and V_m^{DFT} represent specific surface areas and pore volumes as calculated by the HS-2D-NLDFT method.
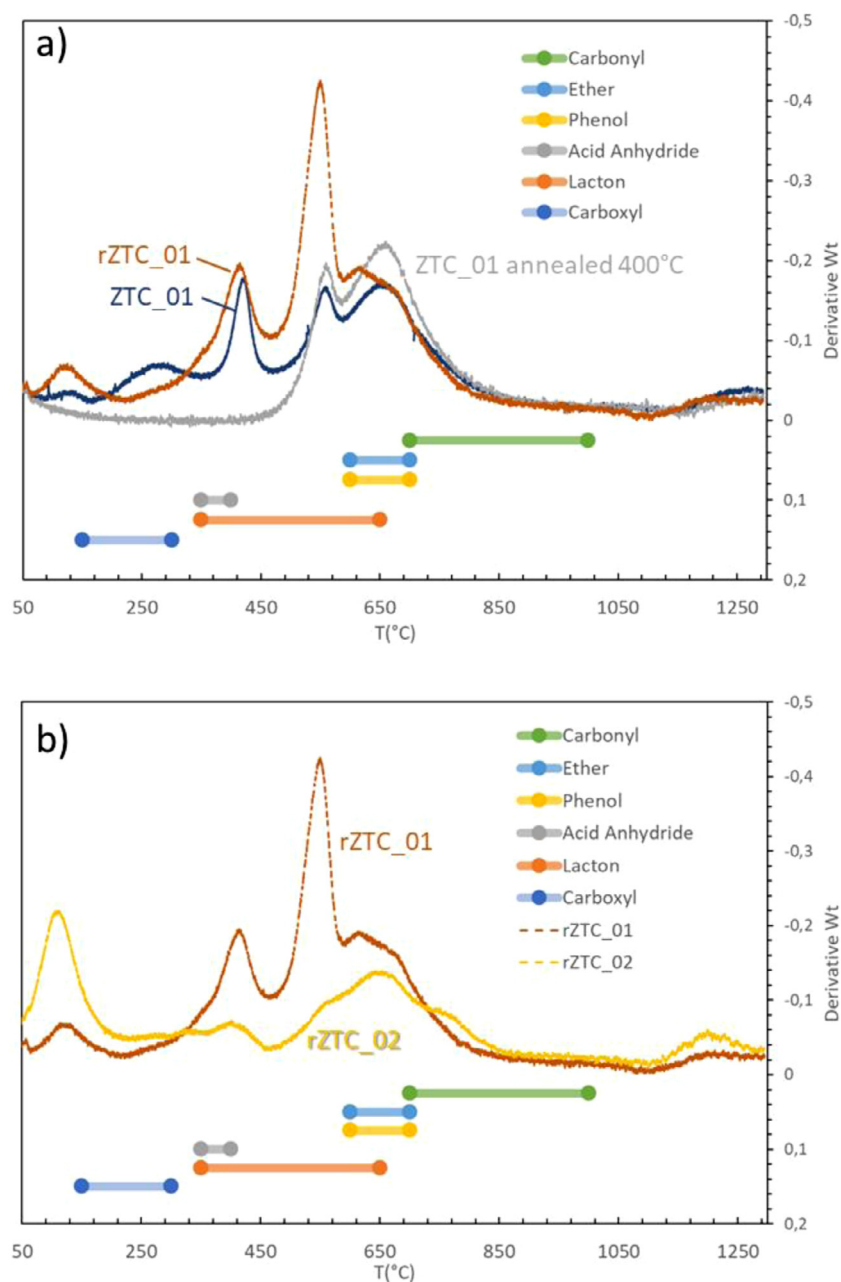
Fig. 5. Derivative of TGA data for ZTC_01 before and after annealing at 400 °C in N$_2$ flow, and after consecutive reduction treatment with NaBH$_4$ (rZTC_01) (a). Comparison of the derivative TGA data for rZTC_01 and rZTC_02 (b). The indicative range of decomposition of oxygenated species in carbon materials according to Nishihara et al. [40] is also presented.
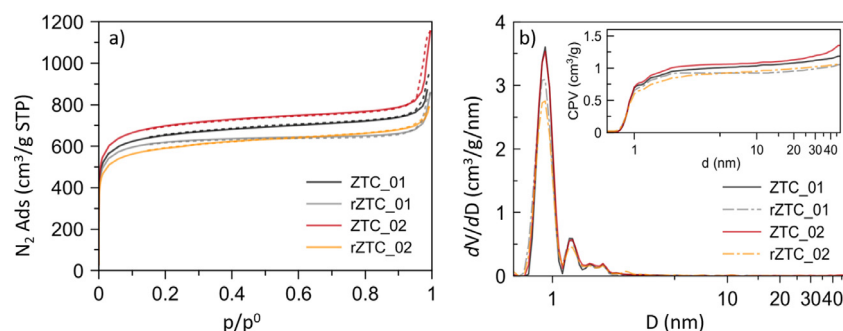
Fig. 6. N$_2$ adsorption isotherms (a) and NLDFT modeling of the N$_2$ physisorption isotherms (b) of the pristine and NaBH$_4$ treated ZTC samples.
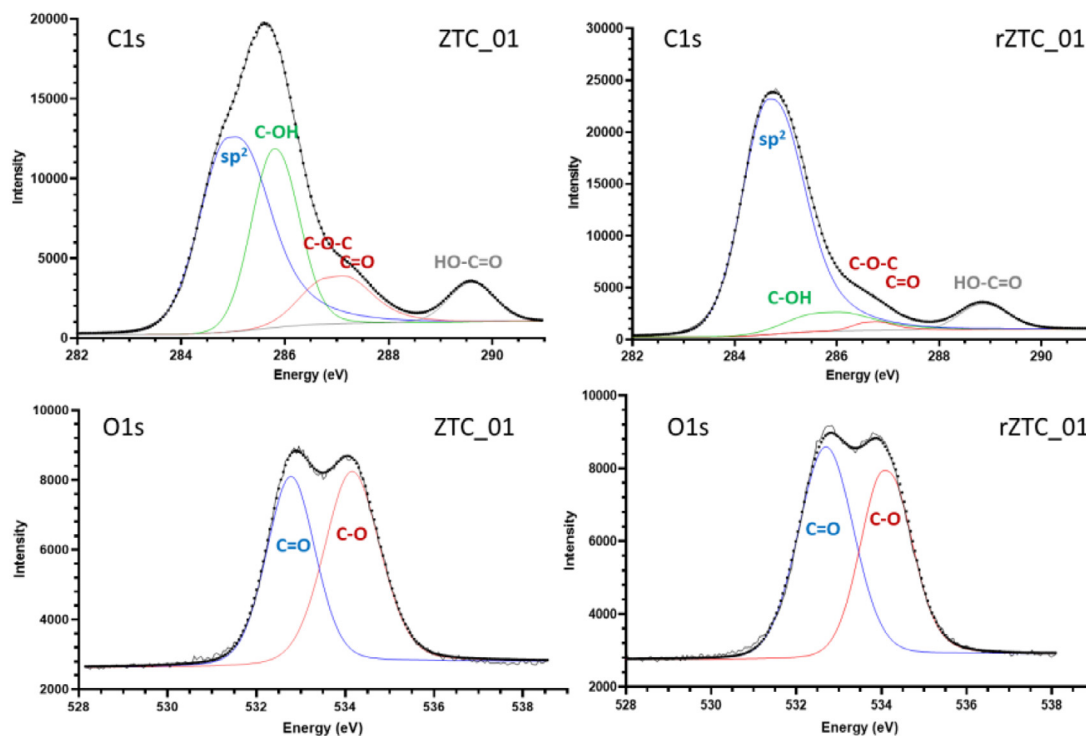

Fig. 7. XPS C1s (top) and O1s (bottom) spectra of ZTC_01 and rZTC_01 samples. The indicative attribution is based on Refs. [35,56,57].

at half maximum (FWHM) associated to the latter pore family did not change significantly. Although only small changes were observed in the micropore diameter, the latter phenomenon can be related to the relaxation of the structure due to the initial annealing treatment and the decreased amount of oxygen and amorphization [55,56]. Moreover, the apparent relative XRD crystallinity of the prepared and treated ZTCs correlated linearly with the total pore volume (V_p, $R^2 = 0.95$) and micropore volume (V_p, $R^2 = 0.85$), in agreement with the micropore network-related crystallinity of ZTCs.

3.2. Spectroscopic characterization

The XPS spectra in the C1s and O1s region of ZTC_01 and rZTC_01 are shown in Fig. 7 with an indicative attribution of the various species obtained by spectral deconvolution, based on indications in Refs. [35,57,58]. The XPS C1s spectrum of the starting ZTC_01 shows the presence of multiple type of carbon species. Together with sp^2 carbon (as would be expected in a material formed by only graphene sheets), various signals associated to sp^3 carbon attributed to different oxygen functionalities are present. The XPS O1s spectrum shows nearly equal intense peaks related to O as-
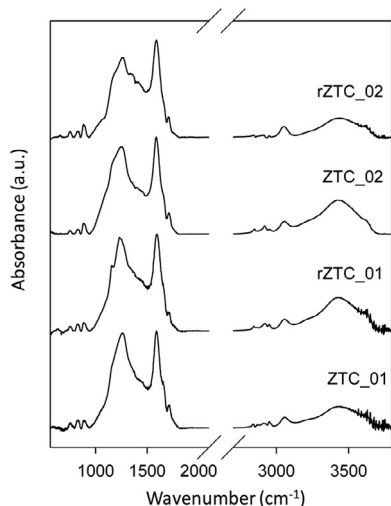
sociated to aliphatic carbon (C–C) and double bonded to carbon. After the thermal annealing and NaBH$_4$ treatment (rZTC_01), the signal related to sp^2 carbon results significantly enhanced, while the others associated to carbon in hydroxyl (C–OH), epoxide (C–O–C) and carbonyl (>C=O) groups remarkably decreased. Moreover, a less extend decrease of carbon associated to carboxyl groups (HO–C=O) was also observed. In XPS O1s spectra a change of the relative intensities of C=O to C–O oxygen species could be consistently observed. Note that fitting by two components well describes the overall O1s spectrum, but being relatively broad, more components (four as those evidenced by Ganguly et al. [57] could also fit the spectrum.

The XPS spectra of ZTC_02 sample before and after the annealing/NaBH$_4$ treatment are similar to those of ZTC_01 series, but the relative intensity of the different components is different. Table 2 reports a summary of the results indicating the relative intensity of the various components in the XPS spectra. As further indexes, the ratio of defective C (as sum of the intensities of components at 285.7, 286.7 and 289.4 eV) to sp^2 carbon (component at 284.8 eV) and of the ratio of C1s signal to O1s signal are shown in Table 2. The data evidence both different characteristics of the starting ZTC sample, and especially of the effect of

Table 2

Relative intensity of the different deconvoluted components in XPS spectra with estimation of the ratio of defective C (as sum of the intensities of components at 285.7, 286.7 and 289.4 eV) to sp^2 carbon (component at 284.8 eV) and of the ratio of C1s signal to O1s signal.

Sample	284.8 eV sp^2 C	285.7 eV (C–C)sp^3 or (C–OH)	286.7 eV C–O	289.4 eV (C=OR)	Ratio defective C to sp^2	C1s/O1s
ZTC_01	51,63	29,98	12	6,39	48,37	4,64
rZTC_01	82,93	8,73	1,89	6,45	17,07	4,78
ZTC_02	61,89	17,1	15,59	5,43	38,12	3,62
rZTC_02	52,65	27,7	13,11	6,54	47,35	1,90

Fig. 8. FT-IR spectra of ZTC samples before and after annealing/NaBH$_4$ treatment.


Fig. 9. FTIR spectra in the 3100–2750 cm^{-1} zone of ZTC_01 and rZTC_01 samples (a) and ZTC_02 and rZTC_02 samples (b).

Fig. 10. Raman spectra of all ZTC samples before and after annealing/NaBH$_4$ treatment.

the annealing/NaBH$_4$ sequential treatment. After this treatment in ZTC_01 there is a decrease of the carbon defective character, although the ratio between C1s/O1s signal only minor change. In ZTC_02 instead the amount of defective carbon increases after the treatment, while nearly doubles the C1s/O1s ratio. The results are consistent with TGA data (Fig. 5).

The FT-IR spectra of the pristine and treated samples are reported in Fig. 8. All samples showed the typical absorption bands of oxygen-containing carbons. More specifically, the broad band in the 3600–3400 cm^{-1} range was attributed to the O-H stretching vibrations [59], while the weak band in the 3100–3000 cm^{-1} range was attributed to the sp^2 C-H bond stretching. The convoluted band in the region 2960–2850 cm^{-1} was attributed to the asymmetric (2930 cm^{-1}) and symmetric (2850 cm^{-1}) stretching of C-H on sp^3 hybridized carbons [60]. The band shown at 1720 cm^{-1} can be assigned to C=O stretching in carboxylic aids, lactones and/or acid anhydrides [41], although its position in aromatic structures can be affected by the presence of the different proximal groups [61].

The band at 1600 cm^{-1} is attributed to the stretching of the sp^2 hybridized carbons [62], while the broad band at 1270–1160 cm^{-1} can be related to the overlapping of C-O-C stretching C-O stretching, and epoxy functional groups [63,64]. More specifically, the bands at 1265 cm^{-1} and 1160 cm^{-1} vibration modes were attributed to the C-O stretch of ether and epoxide groups on the edge sites [65].

After the combined annealing and NaBH$_4$ treatment, the relative intensity of the bands shown at 3000–3100 cm^{-1} and 2890–2940 cm^{-1}, typical of the C-H stretching of sp^2 ($\nu_{C-H_{s,\ sp^2}}$) and sp^3 ($\nu_{C-H_{s,\ sp^3}}$) hybridized carbons, changed with respect to both the pristine samples (Fig. 9). More specifically, from the comparison of the normalized spectra, after the combined annealing and NaBH$_4$ treatment, the intensity of the $\nu_{C-H_{s,\ sp^2}}$ band increases for both ZTCs, indicating a higher surface concentration of these
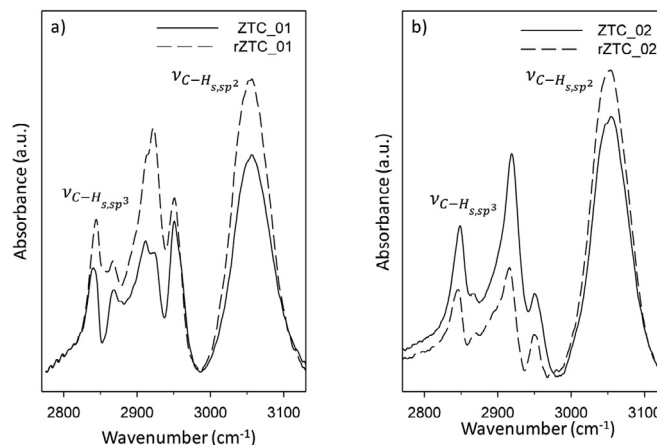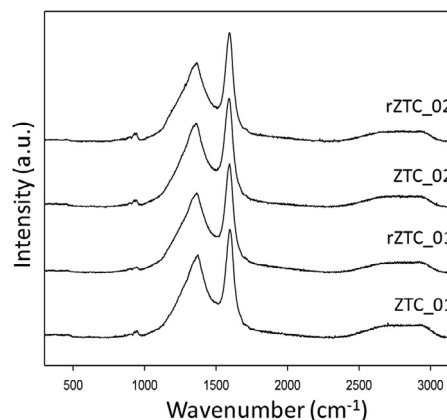
species. Conversely, the $\nu_{C-H_{s,\ sp^3}}$ band of the rZTC_01 shows an increase in comparison to the corresponding pristine sample, while, in the case of the rZTC_02 sample the behavior is reverse. Therefore, FT-IR analysis confirmed that the post-synthesis treatment reduce the amount of oxygen of the samples in comparison to the pristine ones. Moreover, a decrease of the band at 1720 cm^{-1} is observed after the treatment due to the desorption of the carboxylic and lactones induced by the thermal annealing [41] at 400 °C which precedes the NaBH$_4$ treatment and to the partial chemical reduction of acid anhydrides. This decrease is more pronounced for rZTC_01 (Fig. 8).

Because of the resonantly enhanced Raman scattering of carbon materials [66], this spectroscopic analysis has been employed to characterize the modification in the molecular structures of ZTC materials induced by post-synthesis treatments. In Fig. 10 is reported the comparison of Raman spectra for pristine and treated ZTC samples. The Raman spectra of the ZTC samples show the

Table 3

I_D/I_G, I_{D^*}/I_G and $I_{D''}/I_G$ values calculated by five functions deconvolution.

Sample	I_D/I_G	I_{D^*}/I_G	$I_{D''}/I_G$
ZTC_01	1.89	0.66	0.24
rZTC_01	0.75	1.05	0.23
ZTC_02	2.23	0.89	0.55
rZTC_02	1.73	0.73	0.48
rGO	3.26	0.23	0.23
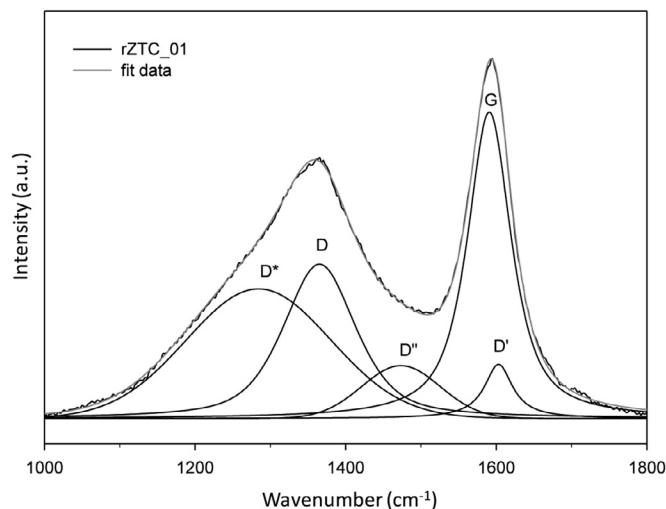
Fig. 11. Example of five functions (D*, D, D″, G, and D′ bands) deconvolution for rZTC_01.

characteristic bands of the graphene based carbons, corresponding to the G band (1580–1600 cm^{-1}) and D-band (1340–1370 cm^{-1}). The first band is associated with the E2g vibration mode of 2D graphite, and D band, is characteristic for the lattice vibration with A1g symmetry and related to the disorder-induced defects in a graphitic structure [67]. Moreover, the measurement of the intensity ratio of the D band to G band, I_D/I_G ratio, allows to assess the disorder and defects in carbon materials [68].

However, the study of the additional contribution of D′, D″ and D* bands, obtained by deconvolution of Raman spectra, using a combination of four Lorentzian and one Gaussian functions allows a more in depth analysis of the degree of order in graphene based carbons [69]. D′ band (around 1620 cm^{-1}) is attributed to the "graphene-like" layers or sp^2 nanostructures with a strained geometry [61], D″ band (around 1500 cm^{-1}), whose intensity is inversely proportional to crystallinity, is observed between the G and D band [70]. The D* band (around 1250 cm^{-1}) is originated from the vibration of carbon sp^3 atoms that were restricted by oxygen-containing groups [69]. When these contributions to the G and D bands are not taken in account, the evaluation of the I_D/I_G ratio due to their superposition, can lead an ambiguous estimation of the degree of order, especially in high-defect density regimes [71].

We analyzed the I_D/I_G ratio values (Table 3) obtained by fitting the Raman spectra using a combination of four Lorentzian and one Gaussian functions. In Fig. 11, the fitting of Raman spectrum through five function (D*, D, D″, G, D′) of rZTC_01 is reported as example. The pristine ZTC_01 and ZTC_02 samples, show a different degree of disorder as evidenced by the values of I_D/I_G ratio, 1.89 and 2.23, respectively. The combined annealing/NaBH$_4$ treatment of the pristine ZTC samples, aimed at the removal of the oxygenated functionalities on the ZTC surface, as expected, leads to the increase of the structural order degree and to the consequent decrease of the I_D/I_G ratio, which is more pronounced for rZTC_01 sample (I_D/I_G = 0.75) whereas for rZTC_02 sample a lower order

degree is reached (I_D/I_G ratio of 1.73). Both the reduced ZTC samples shows a higher degree of order in comparison with the rGO, which presents a I_D/I_G ratio of 3.26.

The analysis of I_{D^*}/I_G and $I_{D''}/I_G$ ratios (Table 3) provides further information regarding the degree of reduction and crystallinity induced by the combined annealing/NaBH$_4$ treatment of the ZTCs samples. Through a combined approach involving the analysis of the Raman spectra changes and theoretical calculation findings, Lee et al. [69] evaluated the degree of reduction (related to the oxygen content of the sample), evidencing also a strict correlation between the intensity ratio of the D* band to the G band (I_{D^*}/I_G) and the C/O atomic ratio. Following the combined annealing/NaBH$_4$ treatment, a decrease in the I_{D^*}/I_G ratio should be expected due to the removal of the oxygenated functionalities (hydroxylic and epoxy groups) bonded to C sp^3 atoms. This trend is confirmed for the sample ZTC_02 for which a decrease in the I_{D^*}/I_G ratio from 0.89 to 0.73 after the treatment. For ZTC_01 we observed an unexpected increase of the I_{D^*}/I_G ratio, indicating the conversion of some sp^2 into sp^3 carbons. This is consistent with the indications from TGA and XPS showing the differences between ZTC_01 and ZTC_02 samples after the annealing/NaBH$_4$ treatment. The annealing of ZTC_01 leads to likely defective carbon species which during the NaBH$_4$ treatment form oxygenated functionalities which could be easily reduced under mild conditions, including vacuum as needed in XPS experiments. For this reason, Raman results show an increase of C sp^3 atoms, while in XPS there is an apparent increase of C sp^2 atoms. In fact, under vacuum the oxygen species may be released reforming sp^2 C atoms. These labile oxygen functionalities, tentatively sp^3 C—OH species [72], are instead not present, or in a minor amount, in rZTC_02 sample, likely due to the different polymorphic nature and zeolite crystal dimensions of the starting Beta zeolite. The Schwarzite structure of Beta-ZTC is characterized by a steeply bent and curved configuration [34], with pentagonal, heptagonal, and octagonal rings in a mostly hexagonal graphene structure. This structure induces partial charge distribution [73] and dangling hydroxyls at the edges creating a dipolar surface. By changing the characteristics of the starting Beta zeolite, reasonably the presence and amount of these defective sites changes [34] and in turn the behavior of the material upon annealing and subsequent NaBH$_4$ treatment.

The $I_{D''}/I_G$ is normally related to the presence of amorphous carbon, and its decrease is normally correlated with an increase of graphene crystallinity [74]. In agreement with the postulated conversion of the amorphous phase into more ordered graphene-like structures, e.g., during the thermal annealing stage, the $I_{D''}/I_G$ ratios observed decrease after the combined annealing/NaBH$_4$ treatment for both samples, with the lowest value observed in the case of the rZTC_02 sample (Table 3), which before this treatment, contains the largest amount of amorphous carbon. To note that the observed decrease in the $I_{D''}/I_G$ ratios is not related by any means to the crystallographic habit of the prepared ZTCs.

Moreover, also the analysis of the shift of the D″ and D* bands to lower or higher wavenumber values, respectively, can provide indication about the decrease of the oxygen content [73]. As further confirmation of the removal of the oxygenated functional groups following the combined annealing/NaBH$_4$ treatment, we observed a shift of the D″ band from 1507 to 1473 cm^{-1} (for rZTC_01) and from 1512 to 1494 cm^{-1} (for rZTC_02), while D* shift from 1255 to 1284 cm^{-1} and from 1253 to 1268 cm^{-1} for rZTC_01 and rZTC_02, respectively (Fig. S.4). The negative shift of D″ observed for both the rZTC_01 and rZTC_02 samples probably indicates the conversion of the amorphous phase to graphene-like structures as a consequence of the treatment. Conversely, the positive shift of the D* band associated with the removal of oxygenated groups in the case of rZTC_01 supports also the indication of the formation of labile sp^3 C-OH species.
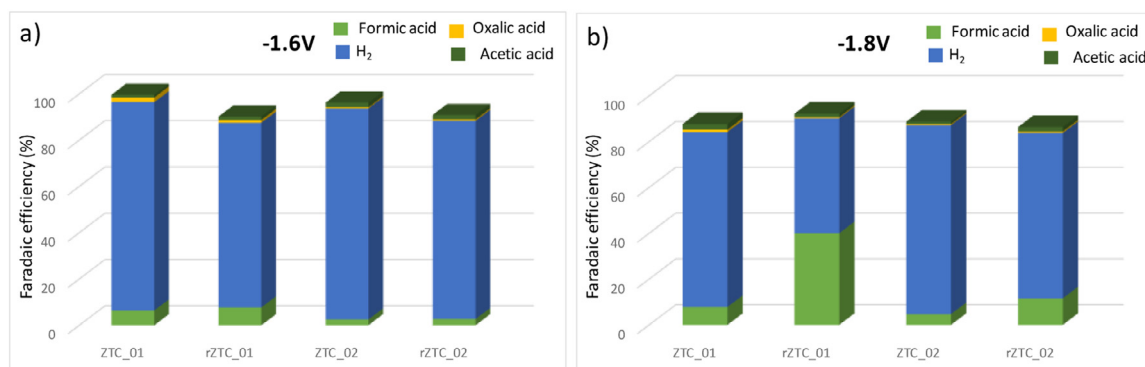
Fig. 12. Faradaic efficiency and CO_2RR products distribution at -1.6 V vs Ag/AgCl (a) and -1.8 V vs Ag/AgCl (b).
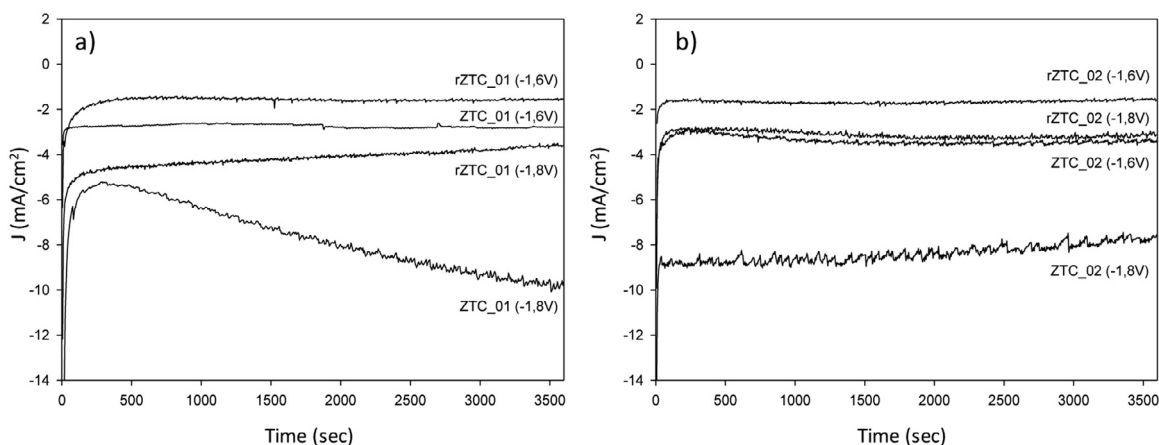

Fig. 13. Chronoamperometry analysis at different applied potentials (-1.6 V and -1.8 V vs Ag/AgCl) in CO_2-saturated 0.5 M $KHCO_3$ solution for ZTC_01 and rZTC_01 samples (a) and ZTC_02 and rZTC_02 samples (b).

3.3. Electrocatalytic activity

ZTC-based electrocatalysts were evaluated in the electrochemical reduction of CO_2 using a commercial flow cell by employing 0.5 M $KHCO_3$ as catholyte and 0.5 M H_2SO_4 as anolyte. For all the tested electrocatalysts, the main product in liquid phase was formic acid (FA), and minor amounts of oxalic acid (OA) and acetic acid (AA) were also detected. The presence of H_2 reveled in the outcoming gas stream can be attributed to the competitive HER (Fig. 12). A possible formation of H_2 from the dehydrogenation of FA is excluded in our reaction conditions (room temperature, low concentration of FA and metal free catalysts), in fact it was reported that the decomposition of FA to H_2 is favored at high temperature, concentrated solution of FA in presence of metal based catalysts [75,76]. To confirm the origin of the liquid products, chronoamperometric control tests were performed at different applied potential (-1.6 V and -1.8 V vs Ag/AgCl) using ZTC based electrocatalysts and by replacing the CO_2 flow with Ar in the $KHCO_3$ electrolyte solution (Fig. S.5). The analysis of the catholyte by HPLC revels that no liquid products deriving from the $KHCO_3$ conversion are revelable and HER is the only reaction under these experimental conditions, as also confirmed by the high amount of H_2 detectable in the gas phase.

The chronoamperometric profiles of all prepared catalysts in CO_2 saturated electrolyte were reported in Fig. 13. As expected, the obtained current density increase with the applied potential, showing that the lower value of current density are reached by using $NaBH_4$ treated ZTC samples compared with the un-treated counterpart, on equal applied potential. The electrocatalysts are stable during the continuos CO_2 electroreduction test under constant po-

tential mode, only for ZTC_01 sample a progressive increase of the current density until a value of 10 mA/cm^2 is observed at -1.8 V (vs Ag/AgCl). Moreover, the comparison of the chronoamperometric profiles both in Ar and CO_2 (Figs. S.5 and 13a), evidences an increase of the current density in the presence of Ar. Most likely, the predominant HER in absence of CO_2, can contribute to this increased current density [77], as also confirmed by the high amount of H_2 detected in the gas phase. These results are also in agreement with the results of cyclic voltammetry in Ar saturated electrolyte (Fig. S.6), which show that the current density is higher at more negative values of potential for all the ZTC samples. Furthermore, the comparison of the cyclic voltammetry in Ar and CO_2 saturated electrolyte for both treated ZTCs samples shows an increase of the current density for rZTC_01 (Fig. S.6b and S.6d).

Faradaic efficiency for FA is higher than those of OA and AA under both -1.6 and -1.8 V (vs. Ag/AgCl) applied potential for all electrocatalysts (Fig. 12). Although more negative potentials favor the HER, an increasing trend in the production of FA was observed by applying a potential of -1.8 V accompanied by a significative decrease of H_2 evolution. The analysis of the results showed that the combined treatment of the pristine ZTC samples significantly improves their electrocatalytic activity, with a variation in the faradaic efficiency to FA passing from 7.8 (ZTC_01) to 40.0% for rZTC_01 and from 4.7% (ZTC_02) to 11.6% for rZTC_02 (Fig. 12). Moreover, in order to assess the effect of the deoxygenation treatment on the two carbon replica (obtained from the two parent zeolites), the combined annealing/$NaBH_4$ treatment was repeated on ZTC_01 and ZTC_02, obtaining two new batches of treated ZTCs, rZTC_01* and rZTC_02*, respectively. The trend in the results obtained for both rZTC_01* and rZTC_02* samples was confirmed,

evidencing no significant differences in the FE towards all detected products ($\pm$ 2%) (Fig. S.7). By using the reference rGO at the same cathodic half-cell potential, we observed a faradaic efficiency towards FA of 3.8%, about 10 times lower than rZTC_01. Analyzing the data obtained and reported in (Fig. S.8), a net decrease in absolute value of the current density is observed for the cyclic voltammetry profiles. Instead, the current density during the chronoamperometric tests at -1.8 V (vs Ag/AgCl) remains at about 4 mA/cm^2, value very similar to those obtained for the electrocatalyst that showed the highest electrocatalytic activity (rZTC_01). This enhancement of the electrocatalytic performance of the ZTC based electrocatalysts, compared to the reference rGO, can be attributed to the accessibility of the active sites due to the higher surface area.

4. Discussion

The ZTCs can be ideally considered as originating from a graphene sheet refolded into the zeolite template channels, giving rise to a 3D, microporous carbon nanostructure with an extremely high surface area. However, the latter strongly depends on the presence of a defective structure with two-sided, ribbon-like "open-blade" connectors [36]. Therefore, these materials can couple the notable characteristics of an electrical conductor, typical of graphene, with the high specific surface of ordered microporous materials, such as zeolites. The co-presence of both these characteristics makes these materials interesting candidates as electrocatalysts for the electrocatalytic reduction of CO_2. However, the strain of the curved structure of graphene inside the nanopores and the ribbon-like "open-blade" connectors leads to the formation of sp^3 carbons, binding oxygenated functional groups. If the presence of the oxygenated groups inside the folded sheet (hydroxylic and epoxidic groups) or on edges (carboxylic acids, lactones and/or anhydrides) decreases the electrical conductivity it should also be considered the role played in the activation of the CO_2 molecule by the presence of these functional groups. On the other hand, the oxygen functionalities on the ZTCs surface may enhance the wettability of the electrocatalysts [78] favoring the diffusion of hydrated CO_2 to active sites and/or the three-phase interfaces [30,79].

The combined annealing and NaBH$_4$ treatment of ZTCs induces a reduction of oxygenated functionalities, but still a significant part appears hard to remove either by thermal annealing and/or subsequent reductive treatment with NaBH$_4$. However, in rZTC_01, differently from rZTC_02, oxygenated species eliminated by the preliminary annealing at 400 °C reform during the treatment with NaBH$_4$, reasonably due to the formation of defective carbon atoms which interact again with water to reform the labile C–OH (sp^3) species. These species are not formed in the case of treated ZTC_02 sample, likely due to the different degree of order in the pristine ZTCs induced by the synthesis conditions (Figs. 4 and 9). As evidenced by the I$_D$/I$_G$ ratio analysis calculated by fitting Raman spectra, the pristine ZTC_01, obtained using the BEA_1 shows a higher degree of order than ZTC_02, prepared from the BEA_2. The NaBH$_4$ treatment increases the degree of order, as evidenced by the reduction of the I$_D$/I$_G$ ratio, to a major extent for the rZTC_01 (Table 3). For the rZTC_02, the increase of the degree of order can be prevalently ascribed to the reduction of the hydroxylic and epoxy groups on the inner surface, as also evidenced by the decrease in the relative intensity of the band at 2930 and 2850 cm^{-1} assigned to sp^3 carbons and the corresponding increase of the band at 3100 cm^{-1} assigned to C–H stretching of sp^2 carbon (Fig. 9b). The analysis of the D* band contribution to the Raman spectra of ZTC samples, originated from the vibration of carbon sp^3 atoms that were restricted by oxygen-containing groups, allowed to evidence an increase of the sp^3 carbon in the rZTC_01 sample following the combined annealing/NaBH$_4$ treatment (Table 3). In agreement, there

Table 4
Variation of the surface oxygenated species of the ZTCs before and after the annealing/NaBH$_4$ treatment.

Sample	C-O-R/C=C [a]	C-OH/C=O [b]
ZTC_01	1.58	3.56
rZTC_01	1,36	5.27
ZTC_02	1,79	3.15
rZTC_02	1,45	2.76

[a] C-O-R/C=C ratio calculated taking into account the area of the bands at 1290–1120 cm^{-1} and at 1580–1660 cm^{-1}.
[b] C-OH/C=O ratio calculated taking into account the area of the bands at 1040–1120 cm^{-1} and at 1710–1760 cm^{-1}.

is an increase of the relative intensity of the band assigned to the symmetrical and asymmetrical stretching of the C-H bond in sp^3 carbon (Fig. 9a) and the decrease of the peak intensity at 1720 cm^{-1} [41]. In order to evaluate the variation of the surface oxygenated species before and after the reducing treatment of the ZTC samples, the C-O-R/C=C ration was calculated (see Supplementary Information), taking into account the area of the bands at 1290–1120 cm^{-1} and at 1580–1660 cm^{-1}. It was assumed constant the C=C band intensity in this estimation, a reasonable assumption due to ZTCs characteristics [61]. The NaBH$_4$ treatment induces variation on the C-O functional groups located on the surface of the ZTC, leading to a consequent decrease in the C-O-R/C=C ratio (which decrease from 1.58 to 1.36 for the samples ZTC_01 and for rZTC_01 and from 1.79 to 1.45 for the samples ZTC_02 and for rZTC_02, respectively) (Table 4). A different trend is highlighted from the analysis of the ratio C-OH/C=O ratio for the two reductive treatments under analysis. Specifically, in the ZTC_01 and rZTC_01, the C-OH/C=O ratio increased from 3.56 to 5.27, respectively. Conversely, in the ZTC_02 and rZTC_02 samples, it decreased from 3.15 to 2.76 (Table 4). This result represents a further confirmation of the Raman evidences from either the analysis of the D* band contribution or the changing in the relative intensity of the band between 3100 and 2800 cm^{-1} typical of the C-H stretching of sp^2 and sp^3 carbons, indicating the formation of defective carbon sites during the treatment and formation of labile CH$_2$–OH groups (sp^3) following the NaBH$_4$ treatment (Table 3 and Fig. 9).

The effects of combined annealing /NaBH$_4$ treatment on the distribution of functional groups of ZTCs samples affected the electrocatalytic performances of the CO_2RR. As discussed in Section 3.3, all ZTCs electrocatalysts showed enhanced activity towards FA compared to the reference rGO, which can be considered a good benchmark for the behavior of metal-free carbon materials containing a large amount of oxygen in the pristine state (GO). It was widely reported that the enhanced conductivity of rGO compared to other 2D or 3D carbon allotropes, is due to the prevalent sp^2 planar structure [80]. This enhancement of the electrocatalytic performance of the ZTCs based electrocatalyst can be then attributed to the accessibility of the active sites due to the higher surface area. As a consequence of the treatment, rZTC_01 showed the highest activity towards FA formation (more than ten times higher than rGO). By analysing the Faradaic efficiency towards FA as a function of the degree of order, measured by I$_D$/I$_G$ ratio, a direct correlation was observed (Fig. 14a), indicating that the electrocatalytic activity of the metal-free carbon electrocatalysts increases with the degree of order whitin the structure. Additionally, it was demonstrated that also the oxygen content of the ZTC electrocatalysts plays a crucial role. In fact, by plotting the Faradaic efficiency towards FA versus the C-O-R/C=C, we observed a decreasing non linear trend when increasing the oxygen content in the samples (Fig. 14b).
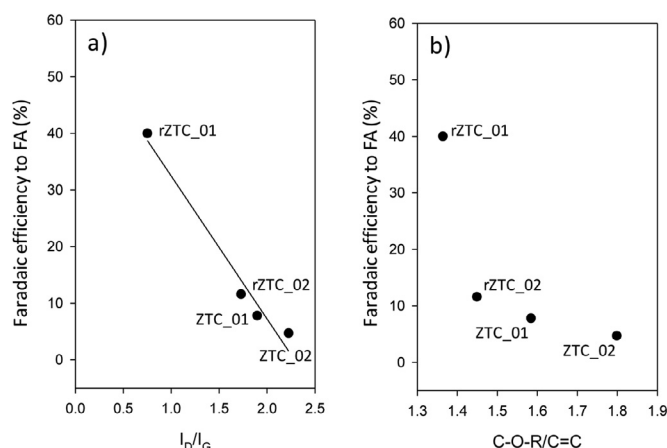
Fig. 14. Correlation between the Faradaic efficiency to FA and the disorder degree of the ZTCs-based electrocatalysts (I_D/I_G obtained by Raman analysis) (a) and C-O-R/C=C ratio calculated by FT-IR (b).

5. Conclusions

This paper presents results in applying ZTCs as electrocatalysts in CO_2 reduction, focusing on the effect of deoxygenation treatments over either the textural properties of the materials or the catalytic performances. Two pristine ZTCs were synthesised using two different BEA templates. They were further modified by a deoxygenation procedure, based on a combination of thermal and $NaBH_4$ treatments. As benchmarking to compare the behavior, a reduced graphene oxide (rGO) was used, being the pristine GO a suitable example of high-oxygen content carbon nanomaterials. ZTCs after the combined annealing/$NaBH_4$ treatment show an apparent loss of crystallinity with a progressive amorphization of the ZTC structure. Textural properties of the samples revealed a progressive reduction of the surface area as the effect of post-synthesis treatment, while the reduction of oxygen content was observed from FT-IR spectra. A deep analysis of Raman spectra gave more details about the disorder of the different ZTC structures, showing an increasing trend of order degree for both treated rZTC_01 and rZTC_02 samples. In addition, the analysis of the deconvolution of D and G bands, highlights the conversion of the amorphous phase into a "graphene-like" ordered one, coupled with a reduction of oxygen content. Results of TGA and XPS characterization were in line with FT-IR and Raman indications. The induced surface modification coherently affected the electrocatalyst activity, with a faradaic efficiency significantly higher for rZTC_01 than for the other samples with a significant correlation of the catalyst performance increase with the increase in structural order and the amount of oxygenated groups on ZTCs. As a final remark, even though the fact that other aspects are still to be investigated in the applications of ZTC electrocatalysis, the work results indicates that the combination of use of ZTCs and their surface modifications are promising ways for innovative CO_2 electrocatalytic reduction processes.

Declaration of Competing Interest

The authors declare that they have no known competing financial interests or personal relationships that could have appeared to influence the work reported in this paper.

CRediT authorship contribution statement

G. Papanikolaou: Conceptualization, Methodology, Investigation, Writing – original draft. **S. Perathoner:** Supervision, Fund-

ing acquisition. **G. Centi:** Supervision, Funding acquisition. **G. Giorgianni:** Investigation, Data curation, Writing – original draft. **M. Migliori:** Supervision, Writing – review & editing. **G. Giordano:** Supervision, Funding acquisition. **P. Lanzafame:** Conceptualization, Methodology, Data curation, Writing – review & editing, Supervision.

Supplementary materials

Supplementary material associated with this article can be found, in the online version, at doi:10.1016/j.apmt.2022.101383.

References

[1] S. Jin, Z. Hao, K. Zhang, Z. Yan, J. Chen, Advances and challenges for the electrochemical reduction of CO_2 to CO: from fundamentals to industrialization, Angew. Chem. 133 (2021) 2–24, doi:10.1002/anie.202101818.

[2] G. Centi, S. Perathoner, Chemistry and energy beyond fossil fuels. A perspective view on the role of syngas from waste sources, Catal. Today 342 (2020) 4–12, doi:10.1016/j.cattod.2019.04.003.

[3] L. Wang, M. Pumera, Electrochemical catalysis at low dimensional carbons: graphene, carbon nanotubes and beyond – a review, Appl. Mater. Today 5 (2016) 134–141, doi:10.1016/j.apmt.2016.09.011.

[4] A. Liu, M. Gao, X. Ren, F. Meng, Y. Yang, L. Gao, et al., Current progress in electrocatalytic carbon dioxide reduction to fuels on heterogeneous catalysts, J. Mater. Chem. A 8 (2020) 3541–3562, doi:10.1039/C9TA11966C.

[5] G. Centi, S. Perathoner, Nanocarbon for energy material applications: N_2 reduction reaction, Small 17 (2021) 2007055, doi:10.1002/smll.202007055.

[6] G. Centi, S. Perathoner, Catalysis for solar-driven chemistry: the role of electrocatalysis, Catal. Today 330 (2019) 157–170, doi:10.1016/j.cattod.2018.03.005.

[7] W. Ma, X. He, W. Wang, S. Xie, Q. Zhang, Y. Wang, Electrocatalytic reduction of CO_2 and CO to multi- carbon compounds over Cu- based catalysts, Chem. Soc. Rev. 50 (2021) 12897–12914, doi:10.1039/D1CS00535A.

[8] G. Wang, J. Chen, Y. Ding, P. Cai, L. Yi, Y. Li, C. Tu, Y. Hou, Z. Wen, L. Dai, Electrocatalysis for CO2 conversion: from fundamentals to value- added products, 50 (2021) 4993–5061. 10.1039/D0CS00071J

[9] A.S. Agarwal, Y. Zhai, D. Hill, N. Sridhar, The electrochemical reduction of carbon dioxide to formate/formic acid: engineering and economic feasibility, ChemSusChem 4 (2011) 1301–1310, doi:10.1002/cssc.201100220.

[10] S. Zhao, S. Li, T. Guo, S. Zhang, J. Wang, Y. Wu, et al., Advances in Sn- based catalysts for electrochemical CO_2 reduction, Nano Micro Lett. 11 (2019) 62–80, doi:10.1007/s40820-019-0293-x.

[11] P. Ding, H. Zhao, T. Li, Y. Luo, G. Fan, G. Chen, et al., Metal- based electrocatalytic conversion of CO_2 to formic acid/formate, J. Mat. Chem. A Mater. Energy Sustain. 8 (2020) 21947–21960, doi:10.1039/D0TA08393C.

[12] W. Zhu, L. Zhang, P. Yang, C. Hu, Z. Luo, X. Chang, et al., Low-coordinated edge sites on ultrathin palladium nanosheets boost carbon dioxide electroreduction performance, Angew. Chem. 130 (2018) 11718–11722, doi:10.1002/ange.201806432.

[13] F. Cai, D. Gao, R. Si, Y. Ye, T. He, S. Miao, et al., Effect of metal deposition sequence in carbon-supported Pd–Pt catalysts on activity towards CO_2 electroreduction to formate, Electrochem. Commun. 76 (2017) 1–5, doi:10.1016/j.elecom.2017.01.009.

[14] R. Arrigo, M.E. Schuster, S. Wrabetz, F. Girgsdies, J.P. Tessonnier, G. Centi, et al., New insights from microcalorimetry on the FeOx/CNT-based electrocatalysts active in the conversion of CO_2 to fuels, ChemSusChem 5 (2012) 577–586, doi:10.1002/cssc.201100641.

[15] Z. Li, D. He, X. Yan, Z.Ke S.Younan, et al., Size-dependent nickel-based electrocatalysts for selective CO_2 reduction, Angew. Chem. 132 (2020) 18731–18736, doi:10.1002/ange.202000318.

[16] A.B. Laursen, K.U.D. Calvinho, T.A. Goetjen, K.M.K. Yap, S. Hwang, H. Yang, et al., CO_2 electro- reduction on Cu_3P: role of Cu(I) oxidation state and surface facet structure in C1- formate production and H_2 selectivity, Electrochim. Acta 391 (2021) 138889–138899, doi:10.1016/j.electacta.2021.138889.

[17] V.S.S. Mosali, X. Zhang, Y. Zhang, T. Gengenbach, S.X. Guo, G. Puxty, et al., Electrocatalytic CO₂ reduction to formate on Cu based surface alloys with enhanced selectivity, ACS Sustain. Chem. Eng. 7 (2019) 19453–19462, doi:10.1021/acssuschemeng.9b04222.

[18] C. Genovese, C. Ampelli, B.C. Marepally, G. Papanikolaou, S. Perathoner, G. Centi, Electrocatalytic reduction of CO₂ for the production of fuels: a comparison between liquid and gas phase conditions, Chem. Eng. Trans. 43 (2015) 2281, doi:10.3303/CET1543381.

[19] D.L.T. Nguyen, M.S. Jee, D.H. Won, H. Jung, H.S. Oh, B.K. Min, et al., Selective CO₂ reduction on zinc electrocatalyst: the effect of zinc oxidation state induced by pretreatment environment, ACS Sustain. Chem. Eng. 5 (2017) 11377–11386, doi:10.1021/acssuschemeng.7b02460.

[20] G.O. Larrazábal, A.J. Martín, S. Mitchell, R. Hauert, J. Pérez-Ramírez, Synergistic effects in silver–indium electrocatalysts for carbon dioxide reduction, J. Catal. 343 (2016) 266–277, doi:10.1016/j.jcat.2015.12.014.

[21] Z. Yang, F.E. Oropeza, K.H.L. Zhang, P-block metal-based (Sn, In, Bi, Pb) electrocatalysts for selective reduction of CO₂ to formate, APL Mater. 8 (2020) 060901.1–060901.26, doi:10.1063/5.0004194.

[22] P. Lamagni, M. Miola, J. Catalano, M.S. Hvid, M.A.H. Mamakhel, M. Christensen, et al., Restructuring metal–organic frameworks to nanoscale bismuth electrocatalysts for highly active and selective CO₂ reduction to formate, Adv. Funct. Mater. 30 (2020) 1910408–1910418, doi:10.1002/adfm.201910408.

[23] J. Qiao, Y. Liu, F. Hong, J. Zhang, A review of catalysts for the electroreduction of carbon dioxide to produce low-carbon fuels, Chem. Soc. Rev. 43 (2014) 631–675, doi:10.1039/C3CS60323G.

[24] Q. Zhai, Y. Pan, L. Dai, Carbon- based metal- free electrocatalysts: past, present, and future, Acc. Mater. Res. 2 (2021) 1239–1250, doi:10.1021/accountsmr.1c00190.

[25] Z. Li, Y. Chen, T. Ma, Y. Jiang, J. Chen, H. Pan, W. Sun, 2D metal- free nanomaterials beyond graphene and its analogues toward electrocatalysis applications, Adv. Energy Mater. 11 (2021) 2101202, doi:10.1002/aenm.202101202.

[26] D.S. Su, S. Perathoner, G. Centi, Nanocarbons for the development of advanced catalysts, Chem. Rev. 113 (2013) 5782–5816, doi:10.1021/cr300367d.

[27] A.G.A. Mohamed, Y. Huang, J. Xie, R.A. Borse, G. Parameswaram, Y. Wang, Metal- free sites with multidimensional structure modifications for selective electrochemical CO₂ reduction, Nano Today 33 (2020) 100891–100908, doi:10.1016/j.nantod.2020.100891.

[28] D.T. Whipple, P.J.A. Kenis, Prospects of CO₂ utilization via direct heterogeneous electrochemical reduction, J. Phys. Chem. Lett. 1 (2010) 3451–3458, doi:10.1021/jz1012627.

[29] Y. Lin, X. Sun, D.S. Su, G. Centi, S. Perathoner, Catalysis by hybrid sp² /sp³ nanodiamonds and their role in the design of advanced nanocarbon materials, Chem. Soc. Rev. 47 (2018) 8438–8473, doi:10.1039/C8CS00684A.

[30] Y. Zou, S. Wang, An investigation of active sites for electrochemical CO₂ reduction reactions: from *in situ* characterization to rational design, Adv. Sci. 8 (2021) 2003579–2003598, doi:10.1002/advs.202003579.

[31] A. Vasileff, Y. Zheng, S.Z. Qiao, Carbon solving carbon's problems: recent progress of nanostructured carbon-based catalysts for the electrochemical reduction of CO₂, Adv. Energy Mater. 7 (2017) 1700759–1700779, doi:10.1002/aenm.201700759.

[32] C. Genovese, C. Ampelli, S. Perathoner, G. Centi, Electrocatalytic conversion of CO₂ to liquid fuels using nanocarbon-based electrodes, J. Energy Chem. 22 (2013) 202–213, doi:10.1016/S2095-4956(13)60026-1.

[33] H. Nishihara, T. Kyotani, Zeolite-templated carbons - three-dimensional microporous graphene frameworks, Chem. Commun. 54 (2018) 5648–5673, doi:10.1039/C8CC01932K.

[34] P. Sazama, J. Pastvova, C. Rizescu, A. Tirsoaga, V.I. Parvulescu, H. Garcia, L. Kobera, J. Seidel, J. Rathousky, P. Klein, I. Jirka, J. Moravkova, V. Blechta, Catalytic Properties of 3D graphene-like microporous carbons synthesized in a zeolite template, ACS Catal. 8 (2018) 1779–1789, doi:10.1021/acscatal.7b04086.

[35] S.K. Lee, H.N Park, J.W. Yoon, K. Kim, S. June Cho, G. Maurin, R. Ryoo, J.S. Chang, Microporous 3D graphene-like zeolite-templated carbons for preferential adsorption of ethane, ACS Appl. Mater. Interfaces 12 (2020) 28484–28495, doi:10.1021/acsami.0c04228.

[36] E.E. Taylor, K. Garman, N.P. Stadie, Atomistic Structures of zeolite-templated carbon, Chem. Mater. 32 (2020) 2742–2752, doi:10.1021/acs.chemmater.0c00535.

[37] H. Nishihara, H. Fujimoto, H. Itoi, K. Nomura, H. Tanaka, M.T. Miyahara, P.A. Bonnaud, R. Miura, A. Suzuk, N. Miyamoto, N. Hatakeyama. A. Miyamoto. K. Ikeda, T. Otomo, T. Kyotani, Graphene-based ordered framework with a diverse range of carbon polygons formed in zeolite nanochannels, Carbon 129 (2018) 854–862 N Y, doi:10.1016/j.carbon.2017.12.055.

[38] H. Park, S. K.Terhorst, R.K. Bera, R. Ryoo, Template dissolution with NaOH–HCl in the synthesis of zeolite-templated carbons: effects on oxygen functionalization and electrical energy storage characteristics, Carbon 155 (2019) 570–579 N Y, doi:10.1016/j.carbon.2019.09.020.

[39] Y. Lin, Z. Feng, L. Yu, Q. Gu, S. Wu, D.S. Su, Insights into the surface chemistry and electronic properties of sp2 and sp3-hybridized nanocarbon materials for catalysis, Chem. Commun. 53 (2017) 4834–4837, doi:10.1039/C7CC02354E.

[40] G. Centi, S. Perathoner, D.S. Su, Nanocarbons: opening new possibilities for nano-engineered novel catalysts and catalytic electrodes, Catal. Surv. Asia 18 (2014) 149–163, doi:10.1007/s10563-014-9172-0.

[41] H. Nishihara, Q.H. Yang, P.X. Hou, M. Unno, S. Yamauchi, R. Saito, et al., A possible buckybowl-like structure of zeolite templated carbon, Carbon 47 (2009) 1220–1230 N Y, doi:10.1016/j.carbon.2008.12.040.

[42] H. Nishihara, K. Imai, H. Itoi, K. Nomura, K. Takai, T. Kyotani, Formation mechanism of zeolite template carbons, Tanso 280 (2017) 169–174, doi:10.7209/tanso.2017.169.

[43] A.Barroso Bogeat, Understanding and tuning the electrical conductivity of activated carbon: a state-of-the-art review, Crit. Rev. Solid State Mater. Sci. 46 (2021) 1–37, doi:10.1080/10408436.2019.1671800.

[44] T. Aumond, J. Rousseau, Y. Pouilloux, L. Pinard, A. Sachse, Synthesis of hierarchical zeolite templated carbons, Carbon Trends 2 (2021) 100014, doi:10.1016/j.cartre.2020.100014.

[45] J. Parmentier, V. Valtchev, L. Gaslain, L. Tosheva, C. Ducrot-Boisgontier, J. Möller, J. Patarin, C. Vix-Guterl, Effect of the zeolite crystal size on the structure and properties of carbon replicas made by a nanocasting process, Carbon 47 (2009) 1066–1073 N Y, doi:10.1016/j.carbon.2008.12.030.

[46] O. Okhay, A. Tkach, Graphene/reduced graphene oxide-carbon nanotubes composite electrodes: from capacitive to battery-type behaviour, Nanomaterials 11 (2021) 1240–1246, doi:10.3390/nano11051240.

[47] S. Ali, A. Razzaq, S.I. In, Development of graphene based photocatalysts for CO₂ reduction to C1 chemicals: a brief overview, Catal. Today 335 (2019) 39–54, doi:10.1016/j.cattod.2018.12.003.

[48] G. Centi, S. Perathoner, R. Arrigo, G. Giordano, A. Katovic, V. Pedulà, Characterization and reactivity of Fe-[Al,B]MFI catalysts for benzene hydroxylation with N₂O, Appl. Catal. A Gen. 307 (2006) 30–41, doi:10.1016/j.apcata.2006.03.018.

[49] G. Papanikolaou, P. Lanzafame, S. Perathoner, G. Centi, D. Cozza, G. Giorgianni, et al., High performance of Au /ZTC based catalysts for the selective oxidation of bio-derivative furfural to 2-furoic acid, Catal. Commun. 149 (2021) 106234–106239, doi:10.1016/j.catcom.2020.106234.

[50] C. Chen, T. Chen, H. Wang, G. Sun, X. Yang, A rapid, one-step, variable-valence metal ion assisted reduction method for graphene oxide, Nanotechnology 22 (2011) 405602–405608, doi:10.1088/0957-4484/22/40/405602.

[51] M. Thommes, K. Kaneko, A.V. Neimark, J.P. Olivier, F. Rodriguez-Reinoso, J. Rouquerol, et al., Physisorption of gases, with special reference to the evaluation of surface area and pore size distribution (IUPAC Technical Report), Pure Appl. Chem. 87 (2015) 1051–1069, doi:10.1515/pac-2014-1117.

[52] J. Jagiello, J. P.Olivier, 2D-NLDFT adsorption models for carbon slit-shaped pores with surface energetical heterogeneity and geometrical corrugation, Carbon 55 (2013) 70–80 N Y, doi:10.1016/j.carbon.2012.12.011.

[53] T. Lu, W. Yan, R. Xu, Chiral zeolite beta: structure, synthesis, and application, Inorg. Chem. Front. 6 (2019) 1938–1951, doi:10.1039/C9QI00574A.

[54] E. Braun, Y. Lee, S.M. Moosavi, S. Barthel, R. Mercado, I.A. Baburin, et al., Generating carbon schwarzites via zeolite-templating, Proc. Nat. Acad. Sci. U. S. A. 115 (2018) E8116–E8124, doi:10.1073/pnas.1805062115.

[55] S. Choi, H. Kim, S. Lee, Y. Wang, C. Ercan, R. Othman, M. Choi, Large-scale synthesis of high-quality zeolite-templated carbons without depositing external carbon layers, Chem. Eng. J. 280 (2015) 597–605, doi:10.1016/j.cej.2015.06.055.

[56] S. Choi, M.A. Alkhabbaz, Y. Wang, R.M. Othman, M. Choi, Unique thermal contraction of zeolite-templated carbons enabling micropore size tailoring and its effects on methane storage, Carbon 141 (2019) 143–153 N Y, doi:10.1016/j.carbon.2018.09.045.

[57] A. Ganguly, S. Sharma, P. Papakonstantinou, J. Hamilton, Probing the thermal deoxygenation of graphene oxide using high-resolution *in situ* X-ray-based spectroscopies, J. Phys. Chem. C 115 (2011) 17009–17019, doi:10.1021/jp203741y.

[58] W. Qi, W. Liu, B. Zhang, X. Gu, X. Guo, D.S. Su, Oxidative dehydrogenation on nanocarbon: identification and quantification of active sites by chemical titration, Angew. Chem. Int. Ed. 52 (2013) 14224–14228, doi:10.1002/anie.201306825.

[59] M. Amin, S. Malekie, N. Ebrahimi, The analysis of linear dose-responses in gamma-irradiated graphene oxide: can FTIR analysis be considered a novel approach to examining the linear dose-responses in carbon nanostructures? Radiat. Phys. Chem. 176 (2020) 109067–109071.

[60] V. Țucureanu, A. Matei, A.M. Avram, V. Țucureanu, A. Matei, A. Marius, et al., Critical reviews in analytical chemistry FTIR spectroscopy for carbon family study FTIR spectroscopy for carbon family study, Crit. Rev. Anal. Chem. 46 (2016) 502–520, doi:10.1080/10408347.2016.1157013.

[61] E. Groppo, F. Bonino, F. Cesano, A. Damin, M. Manzoli, CHAPTER 4. Raman, IR and I.N.S. Characterization of functionalized carbon materials, in: R.S.C. Catal. Ser., (2018), 103–137. 10.1039/9781788013116-00103

[62] B. Sakintuna, Y. Yu, Preparation and characterization of mesoporous carbons using a Turkish natural zeolitic template/furfuryl alcohol system, Microporous Mesoporous Mater. 93 (2006) 304–312, doi:10.1016/j.micromeso.2006.03.013.

[63] M. Jung, K. Ahn, Y. Lee, K. Kim, J. Rhee, J. Tae, et al., Adsorption characteristics of phenol and chlorophenols on granular activated carbons (GAC), Microchem. J. 70 (2001) 123–131, doi:10.1016/S0026-265X(01)00109-6.

[64] K. Krishnamoorthy, M. Veerapandian, K. Yun, S. Kim, The chemical and structural analysis of graphene oxide with different degrees of oxidation, Carbon 53 (2012) 38–49 N Y, doi:10.1016/j.carbon.2012.10.013.

[65] M. Vujkovic, D. Bajuk-Bogdanovic, L. Matovi, M. Stojmenovi, S. Mentus, Mild electrochemical oxidation of zeolite templated carbon in acidic solutions, as a way to boost its charge storage properties in alkaline solutions, Carbon 138 (2018) 369–378 N Y, doi:10.1016/j.carbon.2018.07.053.

[66] L. Bokobza, J.L. Bruneel, M. Couzi, Raman spectroscopy as a tool for the analysis of carbon-based materials (highly oriented pyrolytic graphite, multilayer graphene and multiwall carbon nanotubes) and of some of their elastomeric composites, Vib. Spectrosc. 74 (2014) 57–63, doi:10.1016/j.vibspec.2014.07.009.

[67] S. Reich, C. Thomsen, Raman spectroscopy of graphite, Philos. Trans. R. Soc. A 362 (2004) 2271–2288, doi:10.1098/rsta.2004.1454.

[68] A.C. Ferrari, J. Robertson, Interpretation of Raman spectra of disordered and amorphous carbon, Phys. Rev. B 61 (2000) 14095–14107, doi:10.1103/PhysRevB.61.14095.

[69] A.Y. Lee, K. Yang, N.D. Anh, C. Park, S.M. Lee, T.G. Lee, et al., Raman study of D* band in graphene oxide and its correlation with reduction, Appl. Surf. Sci. 536 (2021) 147990–147996, doi:10.1016/j.apsusc.2020.147990.

[70] S. Vollebregt, R. Ishihara, F.D. Tichelaar, Y. Hou, C.I.M. Beenakker, Influence of the growth temperature on the first and second-order Raman band ratios and widths of carbon nanotubes and fibers, Carbon 50 (2012) 3542–3554 N Y, doi:10.1016/j.carbon.2012.03.026.

[71] M.S. Dresselhaus, A. Jorio, M. Hofmann, G. Dresselhaus, R. Saito, Perspectives on carbon nanotubes and graphene Raman spectroscopy, Nano Lett. 10 (2010) 751–758, doi:10.1021/nl904286r.

[72] A. Lerf, H. He, M. Forster, J. Klinowski, Structure of graphite oxide revisited, J. Phys. Chem. B 102 (1998) 4477–4482, doi:10.1021/jp9731821.

[73] Y. Liu, J. Wilcox, CO_2 adsorption on carbon models of organic constituents of gas shale and coal, Environ. Sci. Technol. 45 (2010) 809–814, doi:10.1021/es102700c.

[74] S. Claramunt, A. Varea, D. López-Díaz, M.M. Velázquez, A. Cornet, A. Cirera, The importance of interbands on the interpretation of the Raman spectrum of graphene oxide, J. Phys. Chem. C 119 (2015) 10123–10129, doi:10.1021/acs.jpcc.5b01590.

[75] K. Tedsree, T. Li, S. Jones, C.W.A. Chan, K.M.K. Yu, P.A.J. Bagot, et al., Hydrogen production from formic acid decomposition at room temperature using a Ag–Pd core–shell nanocatalyst, Nat. Nanotechnol. 6 (2011) 302–307, doi:10.1038/NNANO.2011.42.

[76] M. Mihet, M. Dan, L. Barbu-Tudoran, M.D. Lazar, G. Blanita, Controllable H_2 generation by formic acid decomposition on a novel Pd/templated carbon catalyst, Hydrogen 1 (2020) 22–37, doi:10.3390/hydrogen1010003.

[77] W. Li, M. Seredych, E. Rodríguez-Castellón, T.J. Bandosz, Metal-free nanoporous carbon as a catalyst for electrochemical reduction of CO_2 to CO and CH_4, ChemSusChem 9 (2016) 606–616, doi:10.1002/cssc.201501575.

[78] R. Shi, J. Guo, X. Zhang, G.I.N. Waterhouse, Z. Han, Y. Zhao, et al., Efficient wettability-controlled electroreduction of CO_2 to CO at Au/C interfaces, Nat. Commun. 11 (2020) 3028, doi:10.1038/s41467-020-16847-9.

[79] S. Ghosh, S. Barg, S.M. Jeong, K. Ostrikov, Heteroatom-doped and oxygen-functionalized nanocarbons for high-performance supercapacitors, Adv. Energy Mater. 10 (2020) 2001239–2001282, doi:10.1002/aenm.202001239.

[80] O.C. Compton, S.B.T. Nguye, Graphene Oxide, Highly reduced graphene oxide, and graphene: versatile building blocks for carbon-based material, Small 6 (2010) 711–723, doi:10.1002/smll.200901934.